

**IMPLEMENTATION AND ANALYSIS
OF FMCW RADAR FOR
TARGET DETECTION AND SAR IMAGING**

by

Aiswarya Nair

A thesis submitted to the Faculty of the University of Delaware in partial fulfillment of the requirements for the degree of Master of Science in Electrical and Computer Engineering

Fall 2025

© 2025 Aiswarya Nair
All Rights Reserved

**IMPLEMENTATION AND ANALYSIS
OF FMCW RADAR FOR
TARGET DETECTION AND SAR IMAGING**

by

Aiswarya Nair

Approved: _____
Dennis Prather, Ph.D.
Professor in charge of thesis on behalf of the Advisory Committee

Approved: _____
Hui Fang, Ph.D.
Chair of the Department of Electrical and Computer Engineering

Approved: _____
Pamela M. Norris, Ph.D.
Dean of the College of Engineering

Approved: _____
Gary T. Henry, Ph.D.
Interim Vice Provost and Dean of the Graduate College

ACKNOWLEDGMENTS

I would like to express my sincere gratitude to my advisor, Dr. Dennis Prather, for giving me the opportunity to work on an engaging and challenging project and for motivating me to pursue a thesis. I am thankful for his constant encouragement, for pushing me to think critically and independently, and for providing me with the resources to explore new ideas. I am deeply appreciative of his trust, patience, and belief in my abilities throughout this journey.

I am also grateful to Dr. Shouyuan Shi and Dr. Xiao-Feng Qi for their valuable feedback and discussions, which offered new perspectives and strengthened my understanding of the subject.

My sincere thanks to the members of Phase Sensitive Innovations (PSI) for their support and for providing resources when needed. I would also like to thank all members of the UD-WiSE group for creating a collaborative, friendly, and encouraging work environment that made research an enjoyable experience.

I am immensely thankful to my friends, who have been a constant source of support and encouragement, especially during times when things felt overwhelming. Finally, I wish to express my heartfelt gratitude to my parents and my brother for their unconditional love and support. Their faith in me, even during uncertain times, has been my greatest strength and motivation.

TABLE OF CONTENTS

LIST OF TABLES	vi
LIST OF FIGURES	vii
ABSTRACT	ix
1 INTRODUCTION.....	1
1.1 Contribution.....	3
1.2 Outline.....	4
2 FUNDAMENTALS OF FMCW SIGNAL GENERATION AND PROCESSING.....	5
2.1 FMCW Radar Block Diagram.....	5
2.2 FMCW Principles.....	6
2.2.1 Range Estimation.....	10
2.2.2 Maximum Unambiguous Range.....	11
2.2.3 Range Resolution.....	12
2.2.4 Velocity Estimation in FMCW Radar.....	13
2.2.5 Maximum Detectable Velocity.....	14
2.2.6 Velocity Resolution.....	15
3 APPLICATION OF FMCW RADAR IN SYNTHETIC APERTURE RADAR (SAR) IMAGING.....	16
3.1 SAR Concepts	16
3.2 Transmit and Receive signals.....	21
3.3 Imaging The Data.....	23
3.3.1 Range Doppler Algorithm.....	24
3.3.2 Backprojection Algorithm.....	29
4 EXPERIMENTAL DEMONSTRATION OF RANGE, VELOCITY, AND IMAGING USING FMCW RADAR.....	32
4.1 Experimental Setup	32
4.2 Anechoic Enclosure.....	33
4.3 Radar Board.....	34

4.4	Virtual Array Geometry	35
4.5	Geometry of Transmit and Receive Elements.....	37
4.6	Data Collection and Organization	39
4.7	Experimental Results.....	40
5	SUMMARY	49
5.1	Future Work.....	50
	REFERENCES	54

LIST OF TABLES

Table 4.1: Specifications of the radar systems used in the experiment.....	35
Table 4.2: Comparison of computation times between imaging algorithms.....	44

LIST OF FIGURES

Figure 2.1. System block diagram.....	6
Figure 2.2: FMCW transmit signal.....	7
Figure 2.3: Chirp signal.....	9
Figure 2.4: Doppler representation.....	13
Figure 3.1: SAR system.....	18
Figure 3.2: Modes of SAR (a) Stripmap mode; (b) Spotlight mode	20
Figure 3.3: Interpretation of the Azimuth–Doppler Relationship.....	21
Figure 3.4: Range-Doppler Algorithm flowchart.....	25
Figure 3.5:Backprojection Algorithm	29
Figure 4.3: Experimental setup; (a) Setup block diagram; (b) Experimental setup	33
Figure 4.2: Anechoic Enclosure	34
Figure 4.1: 24 GHz Radar System; (a) 1-Tx 2-Rx; (b) 1-Tx 4-Rx	35
Figure 4.4: Virtual array of TinyRad	37
Figure 4.5: Transmit and receive element geometry.....	38
Figure 4.6: Data cube	40
Figure 4.7: Experiment setup with target kept at 1m distance	41
Figure 4.8: Range profile; (a) Simulated range profile; (b) Collected range profile	42
Figure 4.9: Target imaging; (a) Imaging by Range-Doppler algorithm; (b) Imaging by Backprojection algorithm.....	43

Figure 4.10: Target 1: Reflective surface separated by 1 cm: (a) Reflective surface separated by 1 cm; (b) RDA image; BP image.....	45
Figure 4.11: Target2: Reflective surface separated by 2 cm; (a) Reflective surface separated by 2 cm; (b) RDA image; BP image.....	46
Figure 4.12: Imaging after Beamforming; (a) image using RDA; (b) image using BP	48
Figure 5.1: Comparison of the reference image with beamspace SAR images formed using 1–7 beams.....	52

ABSTRACT

Frequency Modulated Continuous Wave (FMCW) radar systems are compact, energy efficient, and cost-effective, making them highly suitable for both commercial and defense applications. Operating with continuous low-power transmission, these systems enable accurate detection of target range by measuring the time delay between transmitted and reflected signals and target velocity from the Doppler frequency or position change over time.

To increase the spatial resolution of a radar system, which depends on the antenna aperture and signal bandwidth, without adding hardware complexity, Synthetic Aperture Radar (SAR) techniques are integrated into the FMCW framework. This combination enables the development of a compact and lightweight imaging radar capable of achieving high-resolution imagery through motion. In this approach, measurements are collected at multiple spatial positions under the stop-and-go assumption, and image reconstruction is performed using the Range-Doppler and Backprojection algorithms.

This thesis presents both theoretical and experimental investigations into FMCW radar signal generation, range-velocity measurement, and SAR-based imaging. The results demonstrate the effectiveness of FMCW-based SAR for multi-target localization and high-resolution imaging while maintaining a low-cost and power-efficient hardware design.

Chapter 1

INTRODUCTION

Radar, which stands for Radio Detection and Ranging, is an electromagnetic system designed to detect objects and determine parameters such as range and velocity. The system transmits electromagnetic waves into free space, which propagates until they encounter an object. Upon striking an object, a portion of the transmitted energy is scattered, and some is reflected back to the radar receiver as an echo. The time delay between the transmitted and received signals enables estimation of the object's range, while the frequency shift of the returned signal, resulting from the Doppler effect, provides information about the object's velocity.

Radar systems are designed in various configurations to meet specific applications and performance requirements. One of the most fundamental types is the pulse radar system, in which the radar transmits short pulses of electromagnetic signals and then pauses before transmitting the next pulse. By measuring the time interval between transmission, reflection from the target, and reception of the echo, the system can determine the range or distance of the object. Pulse radars with high transmission power can detect objects at ranges exceeding 100 km, making them particularly suitable for long-range surveillance and object tracking applications.

Another prevalent configuration is the Continuous Wave (CW) radar. In this system, the transmitter emits electromagnetic waves continuously at a constant frequency and amplitude. As the transmission and reception occur simultaneously, CW radars cannot directly measure range but can accurately determine the velocity of moving targets by measuring the Doppler frequency shift between the transmitted and received signals that result from the relative motion between the radar and the object. As a result, CW radars are commonly employed in speed measurement and motion

detection applications and are often referred to as Doppler radars.

A Frequency-Modulated Continuous Wave (FMCW) radar combines the advantages of both pulsed and continuous wave radar systems. It transmits a continuous signal whose frequency varies linearly over a set range. The reflected signal is a time-delayed version of the transmitted waveform, resulting in a small frequency difference between the transmitted and received signals, which is used to determine the object's range, while the phase change of the reflected signal over time provides information about the object's velocity. The continuous transmission and reception of signals enable a high signal-to-noise ratio while operating with significantly lower transmitted power compared to pulsed radar systems.

FMCW radar offers several advantages such as:

- High accuracy in measuring short target ranges.
- Simultaneous determination of target range and velocity, with the ability to resolve closely spaced objects.
- Simplified and cost-effective circuitry due to low frequency signal processing.
- Absence of high peak power pulses, making it safer to operate while maintaining precise measurements.
- Continuous transmission and reception enable real-time monitoring and analysis.
- Minimal range measurement error due to linear frequency modulation.

FMCW radar systems were initially developed for military applications during World War II but have since become widely adopted across numerous civilian and industrial domains. They are extensively used in air and marine traffic control for precise range and velocity measurements, as well as in weather monitoring and remote sensing for atmospheric profiling and terrain mapping. In the automotive industry, they serve as a foundational technology for advanced driver-assistance systems (ADAS) and autonomous vehicles, supporting functions such as collision avoidance,

adaptive cruise control, blind-spot detection, and parking assistance.

In applications that require detailed imaging of a surface or scene such as topographic mapping, infrastructure inspection, and environmental monitoring, simple range measurements are insufficient. To achieve fine spatial resolution and reconstruct two-dimensional images, the Synthetic Aperture Radar (SAR) technique is employed. SAR synthesizes a large effective aperture by coherently combining radar returns collected from multiple positions as the radar platform moves. This approach allows the system to achieve high-resolution imaging in both the range and cross-range (azimuth) dimensions, making it a powerful extension of FMCW radar technology for precise surface and target characterization.

1.1 Contribution

This work serves as a foundational study for understanding and implementing radar imaging systems, with a focus on the operation and processing of Frequency-Modulated Continuous Wave (FMCW) radars. The study consolidates information from diverse academic and technical sources, supported by experimental validation and data analysis. The key contributions of this work are summarized as follows.

First, the thesis presents a comprehensive theoretical and experimental investigation of FMCW radar operation, including the derivation of key equations for estimating target range and velocity. The fundamental principles of signal generation, data acquisition, and beat frequency analysis are examined in detail to provide a clear understanding of FMCW radar behavior.

Second, this study explores the application of Frequency-Modulated Continuous Wave radar in SAR imaging, demonstrating how radar data can be processed to form two-dimensional images using algorithms such as the Range-Doppler and Backprojection methods. Both algorithms are implemented and evaluated to understand their respective roles in achieving spatially resolved radar imaging. Experimental results show that the Range-Doppler algorithm provides faster image formation with lower computational complexity, whereas the Backprojection

algorithm produces clearer, higher-resolution images at the expense of greater processing time and computational load.

Finally, the study compares simulated and experimental datasets to assess the performance, accuracy, and computational aspects of the imaging algorithms. The results highlight the strengths and limitations of each approach, providing insights for further development of advanced radar imaging systems.

1.2 Outline

This thesis focuses on the study and analysis of Frequency-Modulated Continuous Wave radar and its application in Synthetic Aperture Radar (SAR) imaging.

Chapter 2 provides the theoretical background of FMCW radar, detailing the principles of signal generation, modulation, and the techniques used for estimating target range and velocity.

Chapter 3 explores the integration of FMCW radar into SAR imaging systems and examines various image reconstruction algorithms. Emphasis is placed on the Range-Doppler Algorithm (RDA) and the Backprojection Algorithm (BPA), including their theoretical foundations and implementation methods.

Chapter 4 outlines the experimental framework established to validate the theoretical models, including hardware configuration, data acquisition, and measurement procedures. Imaging results from both algorithms are presented and analyzed, with a comparative assessment of accuracy, resolution, and computational performance.

Chapter 5 concludes the thesis by summarizing the key findings and outlining potential directions for future research aimed at enhancing FMCW-based SAR imaging. It also highlights how some of the limitations associated with digital processing can be addressed through the development of photonic-based SAR systems.

Chapter 2

FUNDAMENTALS OF FMCW SIGNAL GENERATION AND PROCESSING

Frequency-Modulated Continuous Wave (FMCW) radar is a system that transmits a continuous signal whose frequency is modulated with time while maintaining a constant amplitude. This process, known as frequency modulation, generates a waveform that periodically sweeps across a defined frequency. In this work, a linear modulation technique is used which can be referred to as Linear Frequency Modulation (LFM).

2.1 FMCW Radar Block Diagram

A frequency synthesizer, together with the voltage-controlled oscillator (VCO), generates the linear FMCW signal at the output of the VCO. This signal is then amplified and divided into two paths: one portion is transmitted through the transmit antenna into free space, while the other is directed to the mixer as a reference for down-converting the received signal. The echo reflected from the target is captured and amplified by the receive antenna before being mixed with the reference signal. The resulting intermediate frequency (IF) signal is then band-pass filtered, amplified, and fed into an analog-to-digital converter (ADC). The digitized data is subsequently collected by a host system for further signal processing and analysis. The Figure 2.1 illustrates the block diagram of an FMCW radar system.

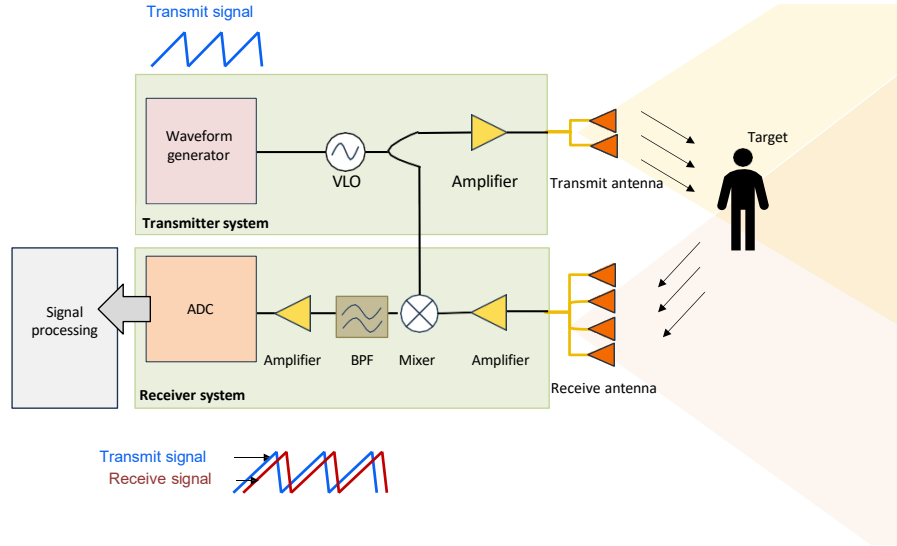


Figure 2.1. System block diagram

2.2 FMCW Principles

The transmitted signal, known as a chirp, is a sinusoidal waveform with a frequency that varies linearly (LFM) over time, producing a continuous frequency sweep across a defined bandwidth (BW). The duration required to complete one frequency sweep is referred to as the chirp duration (T). The instantaneous frequency of the chirp for a time t is defined as:

$$f(t) = f_0 + \beta t , \quad (2.1)$$

where f_0 is the carrier frequency and β is the slope, also known as the chirp rate, which depends on BW and T and is given by:

$$\beta = \frac{BW}{T} . \quad (2.2)$$

A higher slope corresponds to a faster frequency sweep.

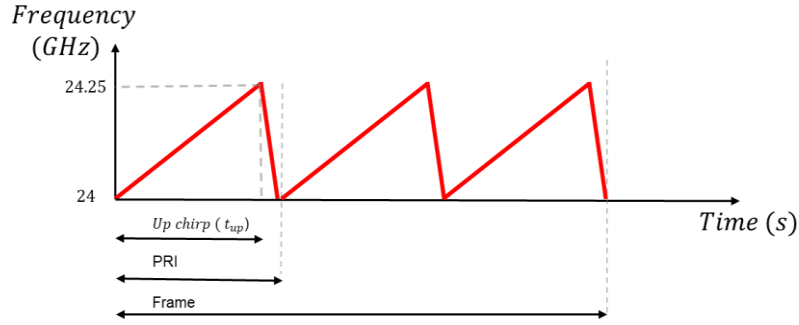


Figure 2.2: FMCW transmit signal

The time duration between two consecutive transmit chirps is called the Pulse Repetition Interval (*PRI*), and its inverse is the Pulse Repetition Frequency (*PRF*):

$$PRF = \frac{1}{PRI} = \frac{1}{T} .$$

In FMCW systems, the *PRI* generally equals the chirp duration T . The received signal is digitized at a rate known as the sampling frequency (f_s), which determines the maximum measurable range and affects the resolution of range processing. The appropriate selection of f_s ensures the accurate capture of the beat signal without aliasing.

The transmitted signal during the first period can be represented as:

$$S_{tx} = \text{rect} \left(\frac{t}{T} \right) \cos(\pi\beta t^2 + 2\pi f_0 t) , \tag{2.3}$$

where

$$\text{rect} \left(\frac{t}{T} \right) = \begin{cases} 1, & |t| \leq \frac{T}{2} \\ 0, & \text{otherwise} . \end{cases}$$

This can be expressed in exponential form by using Euler's identity as:

$$S_{tx} = \text{rect}\left(\frac{t}{T}\right) e^{j(2\pi f_0 t + \pi\beta t^2)} . \quad (2.4)$$

The received signal can be modeled as a time-delayed and attenuated version of the transmitted waveform, with additional system and environmental noise.

$$V_{rx} = \text{rect}\left(\frac{t}{T}\right) e^{j[2\pi f_0(t-\tau) + \pi\beta(t-\tau)^2]} + V_{noise} . \quad (2.5)$$

The time-delay (τ) between the transmitted signal and the received signal is related to the distance (R) between the radar and the target and the propagation speed of the electromagnetic wave, which is taken to be the speed of light (c). Time delay can be shown as:

$$\tau = \frac{2R}{c} . \quad (2.6)$$

In most cases, the range R extends only a few kilometers, resulting in a corresponding time delay on the order of several tens of microseconds.

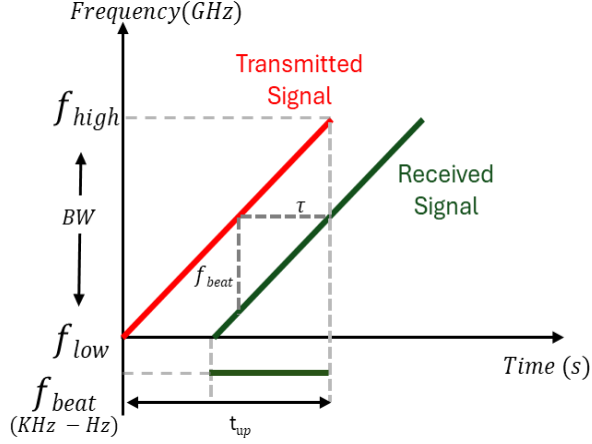


Figure 2.3: Chirp signal

Within the radar receiver, the transmitted and received signals are mixed to generate a down-converted signal called the intermediate frequency (IF) signal. This process is called the de-chirp process. It is expressed as:

$$S_{IF} = \text{rect}\left(\frac{t}{T}\right) e^{j[2\pi f_0(t-\tau) + \pi\beta(t-\tau)^2]} - e^{-j[2\pi f_0 t + \pi\beta t^2]} \quad . \quad (2.7)$$

Simplifying gives:

$$S_{IF} = \text{rect}\left(\frac{t}{T}\right) e^{j[2\pi\beta\tau t + 2\pi f_0\tau - \pi\beta\tau^2]} \quad . \quad (2.8)$$

The first exponential term, $e^{j2\pi\beta\tau t}$, represents the frequency-dependent component. The second and third exponential terms, $e^{j2\pi f_0\tau}$ and $e^{j\pi\beta\tau^2}$, correspond to the phase related components. The third component is small and can generally be ignored,

$$S_{IF} = \text{rect}\left(\frac{t}{T}\right) e^{j[2\pi f_0\tau]} e^{j[2\pi\beta\tau t]} \quad . \quad (2.9)$$

The filtered signal is then digitized using an Analog-to-Digital Converter (ADC) and processed using Digital Signal Processing (DSP) algorithms to extract the target's attributes such as range, angle, and velocity.

2.2.1 Range Estimation

The frequency difference between the transmitted and received signals, known as the beat frequency (f_b), can be used to calculate the target range by directly using the known parameters β and c .

Given a chirp slope β and a time delay τ due to the target's round-trip propagation, the beat frequency (f_b) can be expressed as:

$$f_b = \beta \tau . \tag{2.10}$$

The relationship between beat frequency f_b and target range becomes

$$f_b = \beta \frac{2R}{c} \implies R = \frac{f_b c}{2 \beta} . \tag{2.11}$$

To determine the range (R) of a target using the IF signal (2.9) the frequency-dependent part of the signal is analyzed. To extract this frequency component, a Fast Fourier Transform (FFT) is applied to the IF signal over the fast time, where each sample corresponds to a range bin representing a specific range value. The FFT converts the IF signal from the time domain to the frequency domain, where the dominant peak indicates the distance to the target [1].

By applying continuous time Fourier transform on the IF signal, this can be expressed as:

$$S_{rx} = T \text{sinc}[T(f - \beta\tau)] e^{j[2\pi f_0\tau]} ,$$

(2.12)

where $\text{sinc}(x) = \sin(\pi x)/(\pi x)$ is the *sinc* function, and

$$\text{rect}\left(\frac{t}{T}\right) \leftrightarrow \text{sinc}(Tf) .$$

This can be expanded as:

$$S_{IF} = \frac{1}{2}T\text{sinc}[T(f - \beta\tau)] e^{j2\pi f_0\tau} + \frac{1}{2}T\text{sinc}[T(f + \beta\tau)] e^{-j2\pi f_0\tau} . \quad (2.13)$$

The above equation reveals two symmetric peaks about the Y-axis in the frequency domain representation of $S_{IF}(t)$: the peak at $f = \beta\tau$ appears on the positive frequency side, while the one at $f = -\beta\tau$ lies on the negative frequency side, corresponding to frequency components with opposite phases. In digital signal processing, these peaks appear in the discrete frequency spectrum after performing the FFT and remain symmetric about zero frequency, provided that the zero-frequency component has been properly shifted to the center of the frequency axis. Since both have equal magnitudes but opposite phases, one of them can be discarded without loss of information. Assuming the positive-frequency spectrum is retained, and the negative-frequency component is discarded, we have:

$$S_{IF} = \frac{1}{2}T\text{sinc}[T(f - \beta\tau)] e^{j2\pi f_0\tau} . \quad (2.14)$$

2.2.2 Maximum Unambiguous Range

The maximum unambiguous range defines the farthest distance at which a radar system can uniquely determine a target's position without overlapping from echoes of subsequent chirps. This range primarily depends on the chirp duration T ,

which, for FMCW radar, is equal to the *PRF*. It is also limited by the ADC sampling rate (f_s), since the highest beat frequency that can be measured without aliasing is ($f_s/2$). By setting ($f_b = f_s/2$) and using the relationships established in (2.6) and (2.11), the maximum unambiguous range can be expressed as:

$$R_{max} = \frac{c}{2 \text{ PRF}} , \tag{2.15 a}$$

$$R_{max} = \frac{f_s c}{4 \beta} . \tag{2.15 b}$$

This relationship shows that a higher ADC sampling rate or a smaller chirp slope allows for a larger unambiguous detection range.

2.2.3 Range Resolution

When multiple targets are present within the radar's field of view, the IF signal contains frequency that corresponds to the sum of each target's range. In the frequency domain, these appear as distinct tones, and their separation indicates the relative distances between objects. The radar range resolution defines its ability to distinguish two closely spaced targets, which is possible when the difference between their beat frequencies (Δf_b) exceeds the system's frequency resolution. From the equation (2.2) and (2.11) we get

$$\Delta f_b > \frac{1}{T} \implies \Delta R \frac{c}{c2\beta T} = \frac{c}{2BW} . \tag{2.16}$$

An increase in signal bandwidth (BW) directly enhances range resolution, allowing the radar to resolve objects with smaller separations in range. This can be achieved by increasing the chirp slope, or rate, β or extending the chirp duration T .

2.2.4 Velocity Estimation in FMCW Radar

For a stationary target, the beat frequency corresponds solely to the target's range. However, when the target is in motion, a Doppler shift is superimposed on the beat frequency, allowing the radar to measure both range and velocity. The Doppler frequency (f_d) depends on the relative velocity (v) between the radar and the target and is expressed as:

$$f_d = \frac{2v}{\lambda} \sin \theta \quad , \quad (2.17)$$

where λ is the radar wavelength, R_0 is the shortest distance between the radar and the transmitter and θ is the angle between the radar line-of-sight and the target's direction of motion.

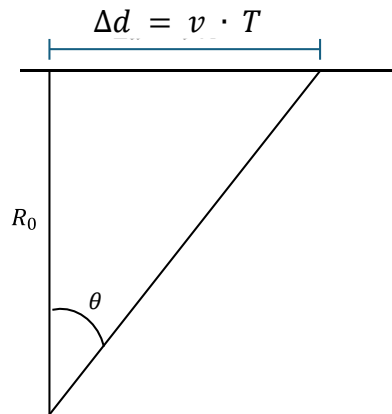


Figure 2.4: Doppler representation

The Doppler effect appears as a phase shift between consecutive chirps and can be expressed using the phase component of equation (2.14). If two consecutive chirps are separated by a time interval T , a target moving with velocity v travels a small distance ($\Delta d = vT$). The corresponding phase difference ($\Delta\phi$) between the received signals of the two chirps is:

$$\Delta\phi = \frac{4\pi\Delta d}{\lambda} = \frac{4\pi vT}{\lambda} . \quad (2.18)$$

Hence, the target velocity can be obtained as:

$$v = \frac{\lambda \Delta\phi}{4\pi T} , \quad (2.19)$$

In practice, the velocity is estimated by performing a Doppler FFT across multiple chirps in the slow-time domain. The resulting Doppler spectrum exhibits peaks corresponding to different target velocities.

2.2.5 Maximum Detectable Velocity

The maximum detectable velocity (also called the unambiguous velocity) is the highest speed that the radar can measure without confusion due to phase wrapping. To avoid ambiguity, the phase difference between two chirps should be less than π . Based on this condition, the maximum velocity, taking ($\Delta\phi = \pi$), that can be measured is:

$$v_{res} = \frac{\lambda}{4T} . \quad (2.20)$$

If a target moves faster than this limit, the radar cannot accurately estimate its direction or velocity without additional signal processing. Therefore, when designing

an FMCW radar, parameters such as the chirp duration T must be carefully chosen to balance the maximum measurable velocity and the velocity resolution.

2.2.6 Velocity Resolution

The velocity resolution defines the smallest difference in velocity that the radar can detect between two moving objects. It depends on the number of chirps in one frame (N) and chirp duration (T). The velocity resolution can be expressed as:

$$\begin{aligned}
 2\pi \frac{2vT}{\lambda} &> \frac{2\pi}{N} \text{ ,} \\
 v_{res} &= \frac{\lambda}{2NT} = \frac{\lambda}{2T_f} \text{ ,} \\
 v_{res} &= \frac{\lambda}{2NT} \text{ .}
 \end{aligned}
 \tag{2.21}$$

Since the total frame time (T_f) is the product of the number of chirps N and the chirp duration T , it can be expressed as: ($T_f = NT$).

Substituting this relationship into (2.23), the velocity resolution can be expressed as:

$$v_{res} = \frac{\lambda}{2T_f}
 \tag{2.22}$$

This shows that the velocity resolution improves (gets finer) when the radar uses more chirps per frame or a longer total frame duration.

Chapter 3

APPLICATION OF FMCW RADAR IN SYNTHETIC APERTURE RADAR (SAR) IMAGING

3.1 SAR Concepts

Accurate positioning of a target in a two-dimensional plane requires both range and cross-range (azimuth) information. The imaging performance of a radar system is primarily determined by two resolution metrics: range resolution and azimuth resolution. The range resolution defines the radar's ability to distinguish between two targets separated along the line of sight and is given by:

$$\Delta R = \frac{c}{2BW} , \tag{3.1}$$

where c is the speed of light and BW is the transmitted signal bandwidth. A larger bandwidth yields finer range resolution, allowing the radar to distinguish closely spaced objects more accurately.

The azimuth resolution, on the other hand, defines the radar's ability to discriminate between two closely spaced objects in the cross-range direction. It depends on the effective synthetic aperture length and can be expressed as:

$$\Delta A = \frac{\lambda R}{L} , \tag{3.2}$$

where λ is the wavelength, R is the range to the target, and L is the aperture length of the radar. A larger aperture provides finer azimuth resolution, which is critical for detailed imaging.

While conventional radar systems can provide precise range measurements, their azimuth resolution at long ranges is inherently poor due to the physical limitations of real-aperture antennas. For example, achieving meter-level azimuth resolution at long ranges would require a real-aperture antenna hundreds of meters long, which is impractical for most airborne or spaceborne radar systems.

The concept of Synthetic Aperture Radar (SAR) overcomes this limitation. One way to understand SAR is from the perspective of antenna arrays. The beam width of a broadside array pattern is inversely proportional to the array length; that is, a longer array produces a narrower beam width and higher angular resolution [2]. The half-power beam width of a broadside array with M elements can be approximated by:

$$\theta_{HPBW} \approx \frac{0.886\lambda}{Md} ,$$

where λ is the wavelength and d is the element spacing. High cross-range resolution can thus be achieved if a sufficient number of elements are available. However, constructing such a large physical antenna is not realistic in most application.

SAR achieves the effect of a large physical antenna by synthesizing it through the motion of a smaller antenna along a linear path. As the radar moves, it sequentially collects echoes from different positions, which are stored and later combined coherently once the platform completes its motion. This coherent Doppler (azimuth) process effectively narrows the azimuth beamwidth, providing resolution equivalent to that of a much larger antenna. The motion-based synthesis forms the foundation of

SAR. Achieving high azimuth resolution depends on maintaining precise phase coherence during data collection, allowing the individual echoes to be combined constructively. Modern SAR systems employ advanced digital signal processing to perform these operations efficiently, enabling real-time or near real-time image formation. This capability makes SAR a vital technology in diverse applications, including remote sensing, defense, environmental monitoring, and disaster response, as it can operate effectively day or night and penetrate clouds and other obstructions.

A SAR operates along two main directions: range and azimuth. The azimuth direction runs parallel to the radar platform's motion and is called the slow-time direction. The range direction, perpendicular to the platform's path and parallel to the radar beam, is known as the fast-time direction. As the platform moves in azimuth, it transmits multiple pulses in the range direction. Each pulse illuminates a footprint, which is the area contributing to the radar back-scatter received by the system.

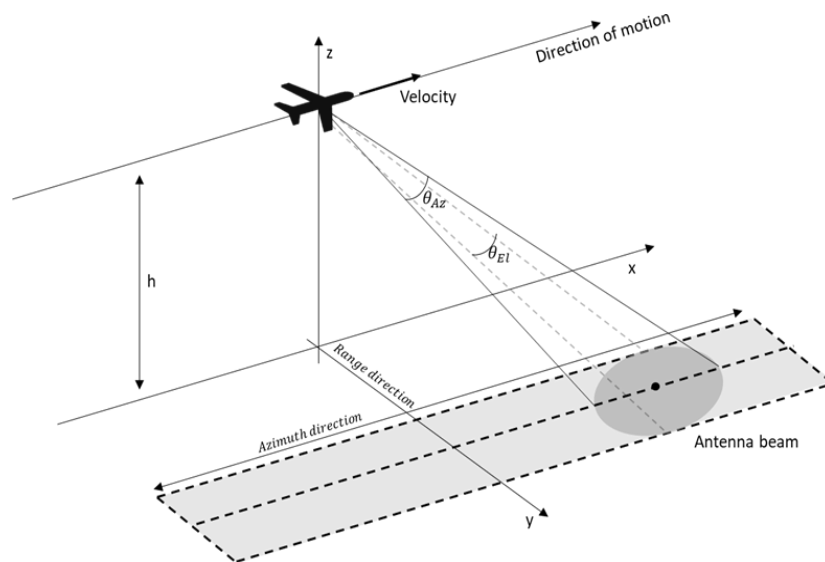
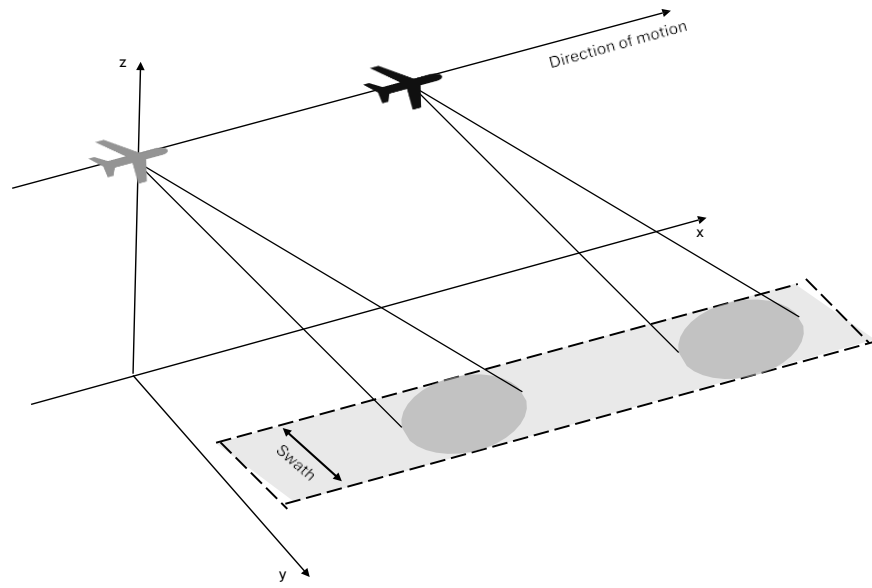


Figure 3.1: SAR system

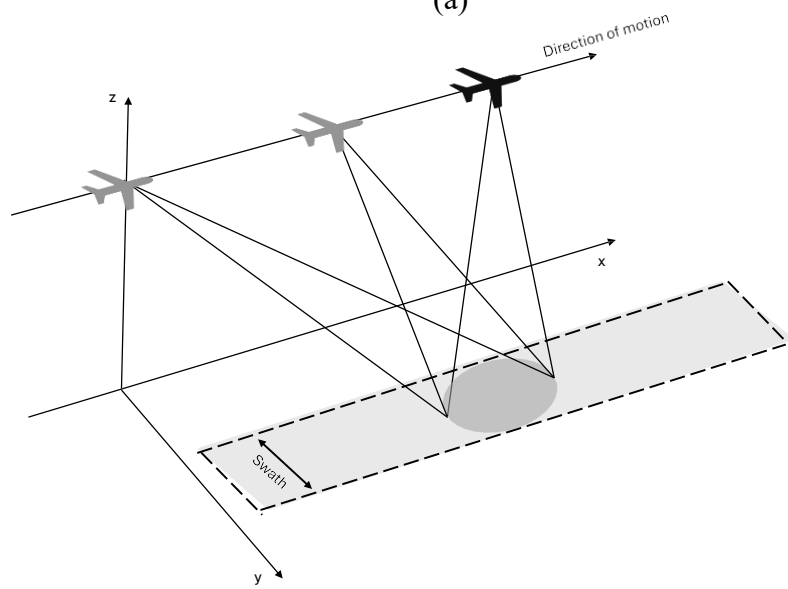
SAR systems primarily operate in three modes as shown in Figure (3.2): stripmap, spotlight, and scan mode. In stripmap mode, the antenna beam remains fixed perpendicular to the flight path throughout the data acquisition. As the radar platform moves, the projection of the antenna beam on the ground traces a continuous strip, and each point within this strip is illuminated for an equal duration. This configuration provides a balanced trade-off between coverage area and resolution and is therefore the most commonly used SAR imaging mode.

In spotlight mode, the antenna beam is actively steered either mechanically or electronically to continuously illuminate a specific region as the platform moves. This allows the radar to observe the target from a wider range of angles, producing images with greater detail and sharper features. Because the radar remains focused on the same spot for a longer period, precise control of the antenna motion is essential to achieve accurate motion compensation and well-focused images. This increased observation time, known as dwell time, enables the collection of more phase-consistent echoes that can be coherently integrated to enhance signal strength and spatial resolution. However, this improvement in image quality comes at the cost of reduced overall scene coverage.

The scan mode increases the radar's coverage area by periodically sweeping the antenna beam across several neighboring sub-swaths as the platform advances. This approach allows the system to image a much wider region, but each ground cell receives less illumination time, leading to lower azimuth resolution. Scan mode is especially valuable for applications that require broad area surveillance, where maximizing coverage is more important than achieving fine detail.



(a)



(b)

Figure 3.2: Modes of SAR (a) Stripmap mode; (b) Spotlight mode

3.2 Transmit and Receive signals

During the SAR operation, the radar transmits an FMCW signal that can be expressed as:

$$S_{tx}(t, \eta) = \text{rect}\left(\frac{t}{T}\right) \text{rect}\left(\frac{\eta - \eta_c}{T_a}\right) e^{j(2\pi f_0 t + \pi \beta t^2)} . \quad (3.3)$$

Here, t represents range time (fast time) and η denotes azimuth time (slow time). β is the chirp slope, or rate, (T_a) represents the synthetic aperture time and f_0 is the carrier frequency. The amplitude of the transmitted signal is assumed to be 1. The time delayed received signal is:

$$V_{rx}(t, \eta) = \text{rect}\left(\frac{t}{T}\right) \text{rect}\left(\frac{\eta - \eta_c}{T_a}\right) e^{j[2\pi f_0(t-\tau) + \pi \beta(t-\tau)^2]} . \quad (3.4)$$

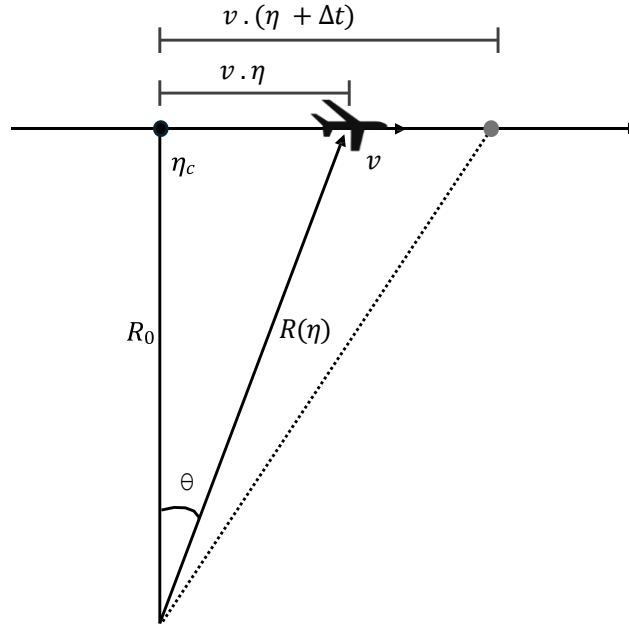


Figure 3.3: Interpretation of the Azimuth–Doppler Relationship

Assume that the radar platform moves horizontally with a constant velocity v , where η denotes the azimuth time (slow time) and η_c is the azimuth time at zero Doppler. A chirp signal is transmitted at each azimuth sampling position, and θ represents the instantaneous incidence angle at each point along the platform's trajectory. R_0 represents the closest slant range between the radar and the target, $R(\eta)$ is the instantaneous slant range at each azimuth position η which is shown as:

$$R(\eta) = \sqrt{R_0^2 + v^2(\eta - \eta_c)^2} . \quad (3.5)$$

The time-delay (τ) between the transmitted and received signal can be taken as:

$$\tau = \frac{2 R(\eta)}{c} = \frac{2}{c} \sqrt{R_0^2 + v^2(\eta - \eta_c)^2} . \quad (3.6)$$

It is assumed that the SAR observes the scene from a broadside. By applying a Taylor series expansion to the square root about ($\eta = \eta_c$) and retaining only terms up to the second order in slow time [1], the expression simplifies as follows:

$$\tau \approx \frac{2}{c} \left(R_0 + \frac{v^2(\eta - \eta_c)^2}{2R_0} \right) . \quad (3.7)$$

As the radar platform moves along the azimuth direction, it continuously transmits and receives signals. Between successive transmissions, the radar advances to a new sampling position, introducing a Doppler frequency shift due to the relative motion between the radar and the target which can be expressed as:

$$2\pi f_d = 2\pi \frac{2v}{\lambda} \sin\theta ,$$

$$f_d = \frac{2v^2\eta}{R\lambda} = K_a \quad , \quad (3.8)$$

where (K_a) denotes the azimuth chirp rate, defined as:

$$K_a = \frac{2v^2}{R\lambda} \quad , \quad (3.9)$$

and (λ) denotes the wavelength,

$$\lambda = \frac{c}{f_0} \quad . \quad (3.10)$$

The IF signal is obtained by mixing the transmitted signal in (3.3) with the received signal given in (3.4), giving:

$$S_{IF}(t, \eta) = \text{rect}\left(\frac{t}{T}\right) \text{rect}\left(\frac{\eta - \eta_c}{T_a}\right) e^{j2\pi f_0 \tau} e^{j2\pi \beta t \tau} e^{j\pi \beta \tau^2} \quad . \quad (3.11)$$

The third exponential term, known as the residual video phase (RVP), is negligible and is thus ignored in subsequent analysis:

$$S_{IF}(t, \eta) = \text{rect}\left(\frac{t}{T}\right) \text{rect}\left(\frac{\eta - \eta_c}{T_a}\right) e^{j2\pi f_0 \tau} e^{j2\pi \beta t \tau} \quad . \quad (3.12)$$

3.3 Imaging The Data

After acquiring data with the SAR system, the information is digitized and processed to reconstruct an image of the target scene. Several signal processing algorithms can be employed for SAR image formation, such as the Range–Doppler

Algorithm (RDA), Backprojection Algorithm (BPA), Chirp Scaling Algorithm (CSA), and Omega-K Algorithm. This thesis focuses primarily on the Range–Doppler and Backprojection algorithms.

3.3.1 Range Doppler Algorithm

The Range–Doppler Algorithm (RDA) was the first imaging algorithm developed for digital SAR signal processing. This method offers computational efficiency by forming SAR images in the range–azimuth frequency domain. The algorithm leverages the significant difference in time scales between the range and azimuth dimensions, allowing the processing to be approximately separated into two independent stages [3]. A key step in this separation is the Range Cell Migration Correction (RCMC), which compensates for the motion-induced curvature of target trajectories in the range–azimuth plane. This correction is performed in the range–frequency and azimuth–frequency domains. Because the azimuth frequency is directly related to the Doppler shift caused by platform motion, the algorithm is named the Range–Doppler Algorithm.

The main steps of the RDA are as follows:

- **Range Compression:** Range compression is performed along the fast-time axis, where the received signals are transformed into the frequency domain using a range FFT.
- **Azimuth Compression:** The range-compressed data are transformed into the range–Doppler domain using an azimuth FFT, aligning signals within the same range bin according to their Doppler characteristics.
- **Range Cell Migration Correction (RCMC):** This step compensates for the range migration of targets by transforming their curved trajectories into straight lines in the range–Doppler domain.

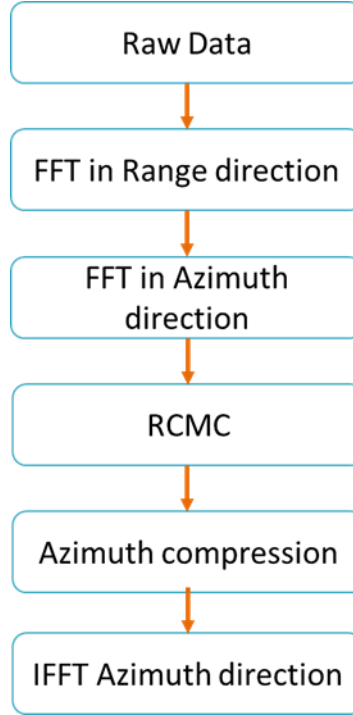


Figure 3.4: Range-Doppler Algorithm flowchart

- **Azimuth Filtering:** Applies matched filtering in the azimuth–frequency domain to achieve azimuth compression.
- **Inverse Azimuth Fourier Transform (IFT):** An inverse FFT along the azimuth dimension transforms the data from the Doppler domain back to the spatial domain.

Applying the range continuous-time Fourier transform (CTFT) to the IF signal in (3.12) and then substituting the time-delay approximation from (3.7), we get:

$$S_{IF}(f, \eta) = T \text{sinc}[T(f - \beta\tau)] \text{rect}\left(\frac{\eta - \eta_c}{T_a}\right) e^{j2\pi f_0 \tau} \quad . \quad (3.13)$$

$$S_{IF}(f, \eta) = Tsinc \left[T \left(f - \beta \frac{2}{c} \left(R_0 + \frac{v^2(\eta - \eta_c)^2}{2R_0} \right) \right) \right] rect \left(\frac{\eta - \eta_c}{T_a} \right) e^{j2\pi f_0 \frac{2}{c} \left(R_0 + \frac{v^2(\eta - \eta_c)^2}{2R_0} \right)}. \quad (3.14)$$

Substituting the value of K_a from (3.9) and wavelength from (3.10) we obtain:

$$S_{IF}(f, \eta) = Tsinc \left[T \left(f - \frac{2\beta R_0}{c} - \frac{\beta v^2(\eta - \eta_c)^2}{cR_0} \right) \right] rect \left(\frac{\eta - \eta_c}{T_a} \right) e^{j\frac{4\pi R_0}{\lambda}} e^{j\pi K_a(\eta - \eta_c)^2}. \quad (3.15)$$

Applying the Fourier Transform (FFT) along the azimuth dimension transforms the signal into the range–Doppler domain.

$$S_{IF}(f, f_\eta) = Tsinc \left[T \left(f - \frac{2\beta R_0}{c} - \frac{\beta v^2(\eta - \eta_c)^2}{cR_0} \right) \right] rect \left(\frac{\eta - \eta_c}{T_a} \right) e^{j\frac{4\pi R_0}{\lambda}} e^{j\pi K_a(\eta - \eta_c)^2} e^{j2\pi f_\eta \eta}, \quad (3.16)$$

where f_η is the azimuth frequency.

By applying the Principle of Stationary Phase (PSP), the approximation can be made as

$$\eta = \frac{f_n}{K_a} + \eta_c, \quad (3.17)$$

$$\eta - \eta_c = \frac{f_n}{K_a}. \quad (3.18)$$

Substituting (3.18) into the Fourier Transform expression and solving yields the following result. Hence, we can write:

$$S_{IF}(f, f_\eta) = Tsinc \left[T \left(f - \frac{\beta 2R_0}{c} - \frac{2\beta}{c} \frac{v^2 f_n^2}{2R_0 k_a^2} \right) \right] rect \left(\frac{\eta - \eta_c}{T_a} \right) e^{j\frac{4\pi R_0}{\lambda}} e^{-j\pi \frac{f_n^2}{k_a}} e^{-j2\pi f_\eta \eta_c}. \quad (3.19)$$

The exponential terms correspond to different phase components of the signal. The first term represents a constant phase, the second is a quadratic term associated with azimuth modulation, and the third is a linear term that determines the azimuth position of the target after azimuth compression [4].

Range Cell Migration and Its Correction

When the IF signals collected from all azimuth positions are converted to the range-frequency domain, through a Fourier transform, the variation in target range between successive transmitted chirps becomes evident. Because of the radar's wide azimuth beamwidth, a target may move through multiple range bins during the synthetic aperture period. This phenomenon is known as Range Cell Migration (RCM). The peak of the *sinc* envelope along azimuth follows a curve that varies with the azimuth frequency (f_η), which can be expressed as:

$$RCM = \frac{\beta v^2 f_\eta^2}{c K_a^2 R_0} .$$

After converting received IF signal into the Doppler-frequency domain, the information collected over the entire synthetic aperture is coherently combined to form a focused image of the target. However, the range variation introduced by RCM complicates this process, as the target's echo energy no longer remains confined within a single range bin. To overcome this issue, the received signal is corrected such that the echo from a single target remains within the same range bin throughout the entire synthetic aperture. This operation is referred to as Range Cell Migration Correction (RCMC) and is typically implemented through interpolation in the range–Doppler domain [4], [5].

After applying RCMC, the signal is compressed in the azimuth direction using an azimuth matched filter. The expression for the azimuth matched filter is given by:

$$H_a(f_\eta) = e^{j\pi\frac{f_\eta^2}{k_a}} \quad . \quad (3.20)$$

After applying (3.20) to the received signal (3.19) the second exponential term is eliminated, yielding

$$S_{IF}(f, f_\eta) = T \text{sinc} \left[T \left(f - \frac{\beta 2R_0}{c} \right) \right] \text{rect} \left(\frac{\eta - \eta_c}{T_a} \right) e^{j\frac{4\pi R_0}{\lambda}} e^{-j2\pi f_\eta \eta_c} \quad . \quad (3.21)$$

Finally, an inverse Fourier transform (IFT) is performed to reconstruct the focused image of the point target.

$$S_{IF}(f, \eta) = A \text{sinc} \left[T \left(f - \frac{\beta 2R_0}{c} \right) \right] \text{sinc}[BW_a(\eta - \eta_c)] e^{j\frac{4\pi R_0}{\lambda}} \quad . \quad (3.22)$$

Here, A represents the signal amplitude. The range and azimuth positions of the target are determined by two sinc functions, whose 3dB widths are $1/T$ and $1/BW_a$, respectively. The azimuth bandwidth (BW_a) depends on the synthetic aperture time (T_a), which is governed by the radar beamwidth and the platform velocity, and is given by:

$$T_a = \frac{L}{v} = \frac{\lambda R_0}{Dv} \quad ,$$

$$BW_a = T_a K_a \quad .$$

3.3.2 Backprojection Algorithm

SAR image formation techniques, such as the Range–Doppler Algorithm (RDA) and other frequency-domain methods, assume that the radar platform follows a straight and uniform path to enable efficient convolution operations using FFTs. Although several modifications exist to account for platform motion deviations, they increase algorithmic complexity and remain limited in performance. In contrast, the backprojection algorithm (BPA) is a time-domain approach that inherently compensates for non-linear trajectories and surface topography variations. It reconstructs the SAR image by directly correlating the received, range-compressed radar echoes with the expected signal from each pixel location [3], [6], [7].

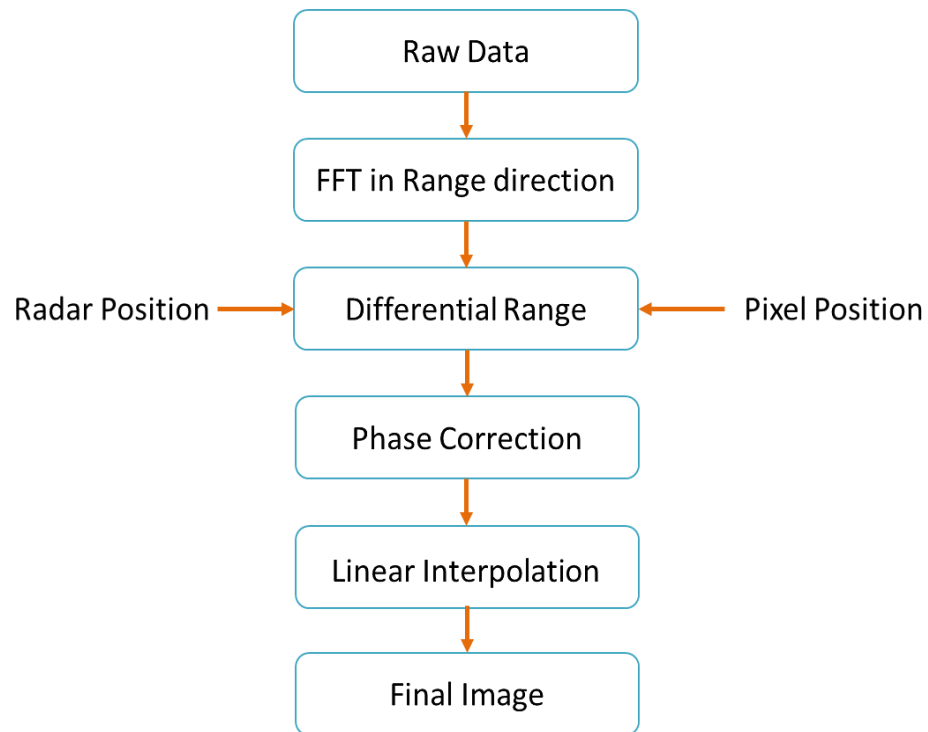


Figure 3.5: Backprojection Algorithm

In the backprojection approach, the radar echo data are first range-compressed to isolate target reflections in fast time. The scene to be imaged is represented as a two-dimensional grid of pixels. For each pixel, the algorithm computes the total propagation distance between the radar and that pixel for every radar position along the aperture. Using this distance, the corresponding time delay and phase shift are determined, allowing the received signal to be properly aligned and phase corrected. The phase-aligned contributions from all radar positions are then coherently summed to estimate the pixel intensity. Repeating this process for every pixel produces a fully focused SAR image.

If the scene to be imaged is represented as a two-dimensional spatial region, with each pixel corresponding to a specific location (x, y) , the intermediate frequency (IF) data received by the radar (3.12) are first range-compressed as in Equation (3.13) to convert the signal from the time domain to the frequency domain, expressed as:

$$S_{IF}(f, \eta) = T \operatorname{sinc} [T(f - \beta\tau)] \operatorname{rect} \left(\frac{\eta - \eta_c}{T_a} \right) e^{j2\pi f_0 \tau} . \quad (3.23)$$

The image is then formed by coherently summing the range-compressed signals across all radar positions:

$$I(x, y) = \sum_{k=1}^N S_{IF}(f, \eta) \left(t = \frac{2R_\eta(x, y)}{c} \right) e^{-j\frac{4\pi R_\eta(x, y)}{\lambda}} , \quad (3.24)$$

where $R_\eta(x, y)$ denotes the distance between the radar position at slow time (η) and the pixel location (x, y) . The exponential term applies the necessary phase correction corresponding to the propagation delay.

The backprojection algorithm provides excellent geometric flexibility and image fidelity. It allows motion compensation on a pulse-by-pulse and pixel-by-pixel basis, making it well-suited for complex flight paths and topography-dependent imaging. However, these advantages come at the cost of high computational complexity and the need for accurate knowledge of radar geometry and motion parameters. Since the algorithm operates directly in the spatial domain, it requires evaluating distances and phase terms for every pixel and every pulse.

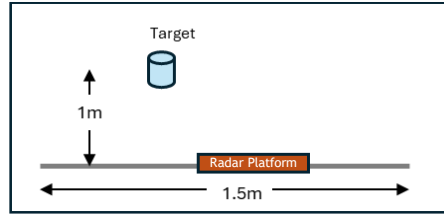
Chapter 4

EXPERIMENTAL DEMONSTRATION OF RANGE, VELOCITY, AND IMAGING USING FMCW RADAR

4.1 Experimental Setup

The experiment was conducted in a controlled laboratory environment equipped with RF absorbers to minimize unwanted reflections and reduce noise in the received signals. The measurement setup consisted of an FMCW radar mounted on a movable platform that traversed a 1.5-meter linear rail. The radar's motion was automated using an Arduino-based control system. A cylindrical target was positioned approximately 1 meter from the rail during the experiment.

Data collection was performed using the stop-and-go method, in which the radar platform halted at discrete positions along the rail to acquire measurements before advancing to the next point. At each position, the radar transmitted and received signals were recorded as in-phase and quadrature (IQ) data. Following the acquisition, the signals were digitized and processed using digital signal processing techniques. Image reconstruction was performed using both the Range-Doppler Algorithm and the Backprojection Algorithm.



(a)



(b)

Figure 4.3: Experimental setup; (a) Setup block diagram; (b) Experimental setup

4.2 Anechoic Enclosure

To minimize unwanted reflections and multi-path effects caused by metallic fixtures in the laboratory, which can introduce noise into the collected data, a semi-enclosed anechoic chamber was constructed. The setup consisted of RF absorber panels arranged around the radar measurement area to suppress stray reflections and simulate a free-space environment. The absorber walls were positioned approximately 3 m from the transmitter-receiver assembly, forming a partial enclosure. The structure was built using aluminum-backed foam boards that served as mounts for 2 ft × 2 ft absorber tiles. Each board held six tiles, attached via a hook-and-loop Velcro system,

with the loop fabric bonded to the panel backs and the hook fabric adhered to the foam boards. The boards were wedged securely between the floor and ceiling to ensure stability, and additional absorber panels were installed where necessary to achieve full coverage of the designated test area.



Figure 4.2: Anechoic Enclosure

4.3 Radar Board

The experiments were conducted using two commercial off-the-shelf radar systems. The first is the Position2Go radar module from Infineon Technologies, featuring one transmit and two receive channels (1Tx–2Rx). It operates in the 24–24.25 GHz band with a bandwidth of approximately 200 MHz.

The second system used in this study is the TinyRad radar module from Analog Devices, configured with two transmit and four receive channels (2Tx–4Rx) and operates in the same 24–24.25 GHz frequency range with 200 MHz bandwidth. The specifications of both radar systems are summarized in Table 4.1.



(a)



(b)

Figure 4.1: 24 GHz Radar System; (a) 1-Tx 2-Rx; (b) 1-Tx 4-Rx

Table 4.1: Specifications of the radar systems used in the experiment

Parameter	1Tx-2Rx	2Tx-4Rx	Unit
Antenna Gain (G)	12	12.6	dBi
Sidelobe Suppression (ΔS)	-20	-20	dB
Horizontal 3dB Beamwidth (θ_H)	76	76.6	degrees
Vertical 3 dB Beamwidth (θ_V)	19°	17.6	degrees
Supply Voltage	5	5	V
Maximum RF Output Power	10.26	8	dBm
Transmit Frequency Range	24–24.25	24–24.25	GHz

4.4 Virtual Array Geometry

When multiple transmit (Tx) and receive (Rx) antennas are co-located, the combination of their positions forms what is known as a virtual array. This represents

a mathematically equivalent configuration that models the behavior of a larger physical array, thereby improving spatial resolution and imaging performance while maintaining compact structure. Each transmitter–receiver pair contributes one virtual element, effectively extending the system's aperture [8].

The position of each virtual element can be expressed as the sum of the spatial coordinates of the corresponding transmitter and receiver elements:

$$d_{mn} = X_m + X_n \quad , \quad (4.1)$$

where X_m and X_n denote the positions of the m^{th} transmitter and n^{th} receiver, respectively.

Example: TinyRad 2 Tx – 4 Rx Configuration:

The TinyRad radar system used in this experiment consists of two transmitters and four receivers arranged linearly. The two transmit antennas are separated by a distance of $\frac{3\lambda}{2}$ while the receiver elements are spaced uniformly at $\frac{\lambda}{2}$ intervals. The first receiver (Rx_1) receives the signal from the first transmitter (Tx_1), which serves as the reference element. Signals received by the subsequent receivers (Rx_2, Rx_3, Rx_4) from the same transmitter experience phase delays proportional to their spacing relative to (Rx_1), resulting from the additional propagation distance introduced by their physical separation.

The two transmitters are separated by $\frac{3\lambda}{2}$ causing signals from Tx_2 to travel an extra distance of about $\frac{3\lambda}{2}$ before reaching the target. This extra path length increases the delay observed at each receiver and shifts the positions of the corresponding virtual elements. Consequently, each unique Tx-Rx pair forms a distinct virtual

element, resulting in a denser effective aperture. When two virtual elements coincide spatially, the overlapping locations are considered redundant. Thus, the spatial arrangement of the transmit and receive antennas in the TinyRad radar system results in a seven-element virtual array [8].

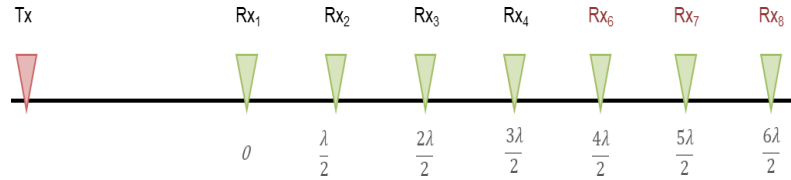


Figure 4.4: Virtual array of TinyRad

4.5 Geometry of Transmit and Receive Elements

To model the geometry of a multiple, transmit multiple receive radar array, it is necessary to define the spatial positions of the transmitting and receiving antenna elements. In a radar system consisting of M transmitter and N receiver elements arranged linearly with uniform spacing, let (d_t) denote the separation between adjacent transmitters and (d_r) the spacing between adjacent receivers. The offset between the first transmitter and the first receiver is defined as (X_{TRx}) . The propagation distance from the first transmitter element to the target, denoted $(R_{TX,1})$, is taken as the reference range [9]. The positions of the remaining elements are then expressed relative to this reference point as:

$$X_m = (m - 1)d_t, \quad \text{for the } m^{\text{th}} \text{ Tx element,}$$

$$X_n = X_{TRx} + (n - 1)d_r, \quad \text{for the } n^{\text{th}} \text{ Rx element.}$$

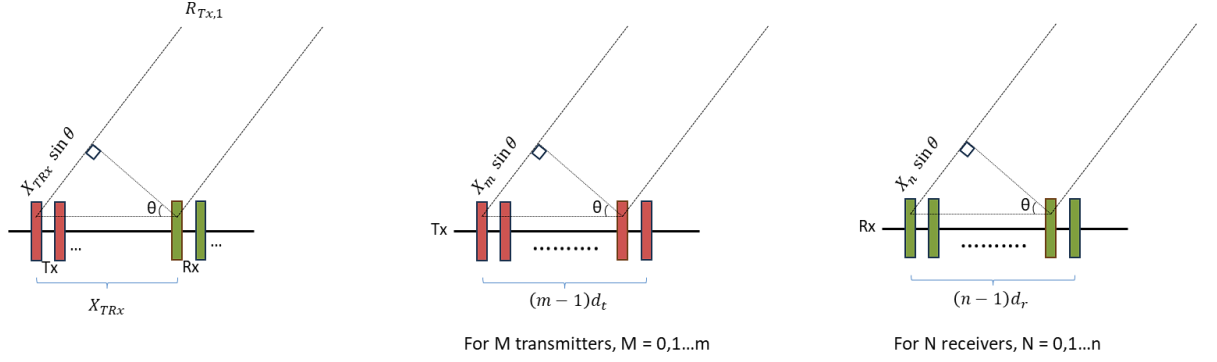


Figure 4.5: Transmit and receive element geometry

Under the far-field approximation, where the distance to the target R_0 is much greater than the array aperture, the propagation distances from each transmitter and receiver to the target are given by:

$$\begin{aligned}
 R_{TX,1} &= \sqrt{R_0^2 + (x_{st} + v_0 \eta)^2} \approx R_{\text{ref}} \quad , \\
 R_{TX,m} &= \sqrt{R_0^2 + ((x_{st} - X_m) + v_0 \eta)^2} \approx R_{\text{ref}} - x_m \sin(\theta) \quad , \\
 R_{RX,n} &= \sqrt{R_0^2 + ((x_{st} - X_n) + v_0 t_s)^2} \approx R_{\text{ref}} - x_n \sin(\theta) \quad ,
 \end{aligned}
 \tag{4.1}$$

where $(x_{st} + v_0 \eta)$ represents the motion of the radar platform, and θ is the target's angle relative to the array broadside.

The total round-trip propagation distance for a signal transmitted from the m^{th} Tx element and received by the n^{th} Rx element is given by:

$$R = R_{TX,m} + R_{RX,n}$$

$$\begin{aligned}
&= R_{\text{ref}} - X_m \sin(\theta) + R_{\text{ref}} - X_n \sin(\theta) \\
&= 2R_{\text{ref}} - (X_m + X_n) \sin(\theta) .
\end{aligned}$$

By using Equation (4.1), the expression can be simplified to:

$$R = 2R_{\text{ref}} - d_{mn} \sin(\theta) . \quad (4.2)$$

The variation in path length across different Tx–Rx pairs introduce phase differences in the received signals, enabling techniques such as beamforming, angle-of-arrival (AOA) estimation, and SAR imaging.

4.6 Data Collection and Organization

The data collected by the radar at each position along the rail are organized into a three-dimensional matrix, commonly referred to as a data cube. This data cube serves as the foundation for estimating key target parameters such as range, velocity, and azimuth angle.

Data Cube Structure

The 3D of the data cube corresponds to distinct domains of radar measurement:

- **Samples** (Fast Time, t):
This dimension represents the temporal samples of the received signal for each transmitted chirp.
- **Pulses** (Slow Time, η)
This dimension represents the sequence of radar pulses collected as the antenna moves along the azimuth direction.
- **Channels** (n)
This dimension corresponds to the number of receiver elements (Rx) in the

radar array. Each receiver provides a spatially distinct observation of the reflected wavefront.

The data cube can therefore be represented as:

$$DC(t, \eta, n) .$$

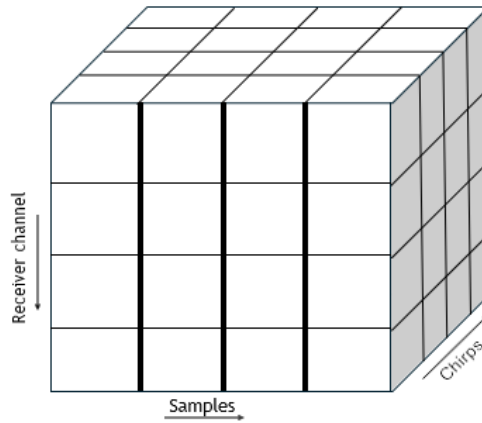


Figure 4.6: Data cube

Each measurement across fast time and receiver channels forms a single slice of the data cube. As the radar platform moves along the rail and repeats this process, successive slices populate the cube along the slow-time dimension. Once data from all positions have been acquired, the data cube is fully populated and ready for subsequent signal processing and image reconstruction.

4.7 Experimental Results

Using the experimental setup described in the previous section data were collected at discrete positions along the rail to form a complete synthetic aperture. The

target was placed approximately 1m from the radar. The experiments were conducted by position2go radar system.

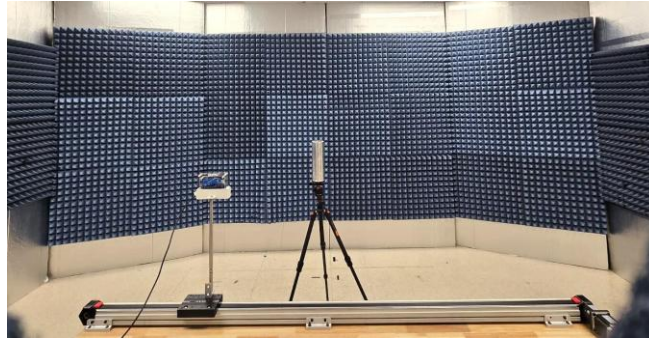
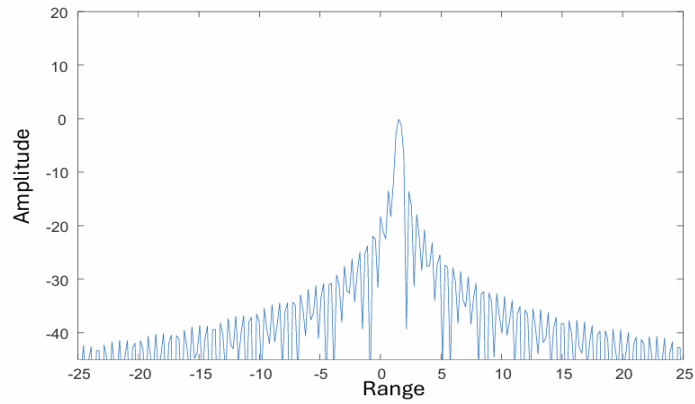


Figure 4.7: Experiment setup with target kept at 1m distance

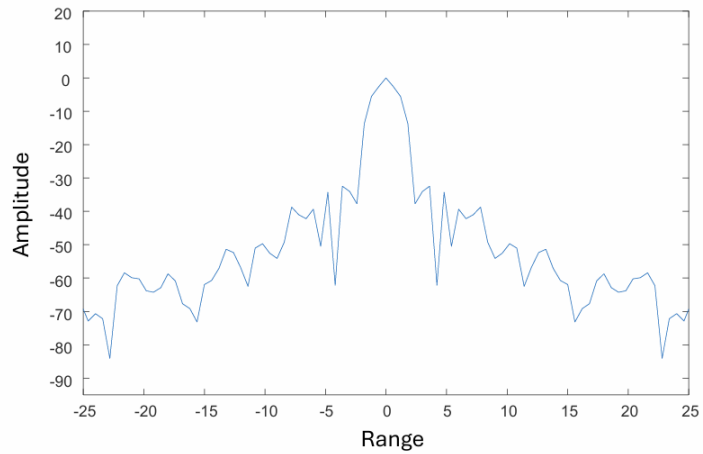
Range Estimation

To estimate the target's range, a Fast Fourier Transform (FFT) was applied to the received IF signal. The FFT converts the signal from the time domain to the frequency domain, where each frequency component corresponds to a specific range bin. The resulting range profile exhibits a distinct peak at the location corresponding to the target's distance from the radar.

Figure (4.8) shows the magnitude of the FFT output, clearly indicating a strong reflection peak at approximately 1m range, consistent with the actual target position. This confirms the correct operation of the radar system and validates the data for subsequent imaging steps.



(a)



(b)

Figure 4.8: Range profile; (a) Simulated range profile; (b) Collected range profile

Imaging Target

The acquired data were processed using two imaging algorithms: the Range–Doppler Algorithm (RDA) and the Backprojection Algorithm (BPA). Both methods were applied to the same dataset for comparison.

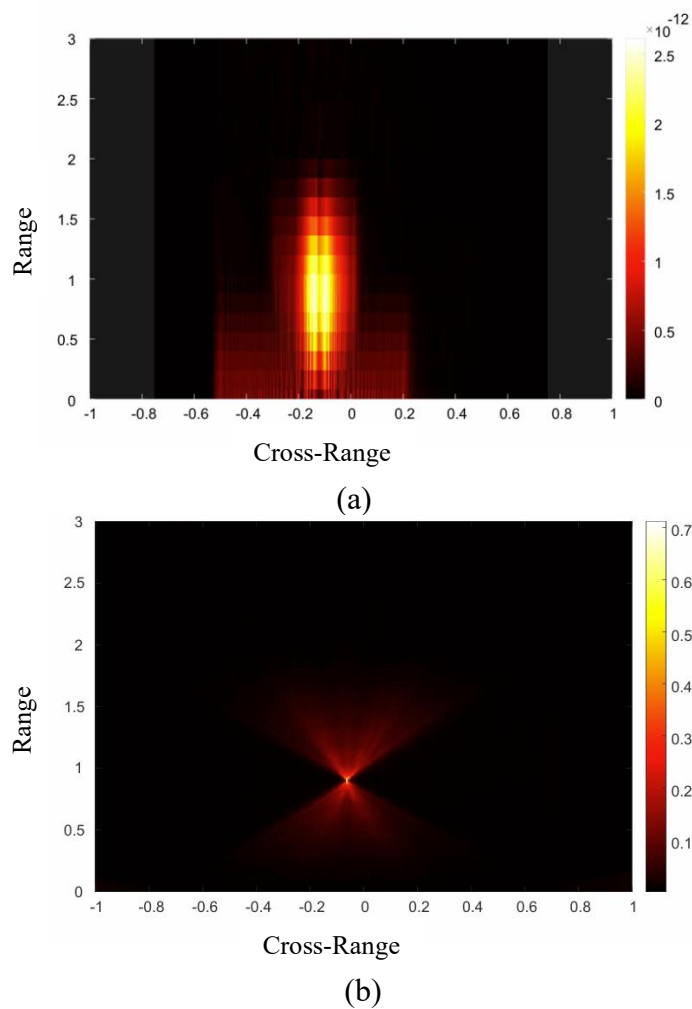


Figure 4.9: Target imaging; (a) Imaging by Range-Doppler algorithm; (b) Imaging by Backprojection algorithm (*figure generated using equations provided by Noah Butler*).

Although the RDA produced a recognizable target image, it exhibited limited spatial resolution. In contrast, the backprojection result provided a much clearer and more focused image of the target, demonstrating its effectiveness in accurately reconstructing the scene. However, this improvement in image quality came at the cost of significantly higher computational complexity and processing time.

To quantify this difference, Table 4.2 summarizes the computation times for each algorithm under identical processing conditions. The results highlight the trade-off between computational efficiency and image quality. While the backprojection algorithm provides superior reconstruction accuracy, its higher processing cost makes it less suitable for real-time applications compared to the Range–Doppler approach.

Table 4.2: Comparison of computation times between imaging algorithms

Algorithm	Computation Time (s)
Range–Doppler Algorithm (RDA)	1.2444
Backprojection Algorithm (BPA)	5.8849

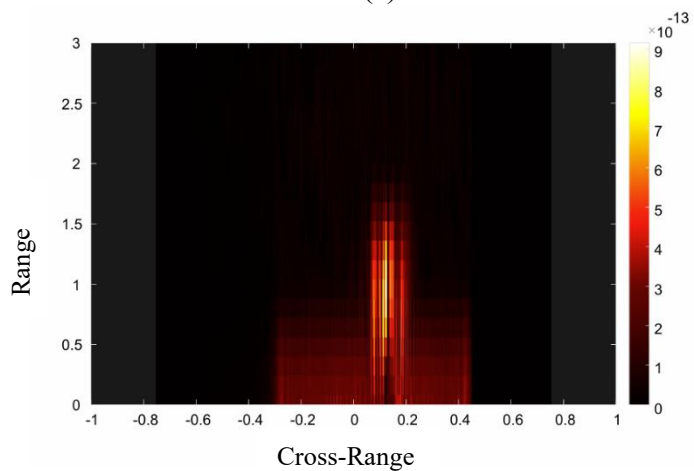
Imaging of Closely Spaced Targets

An experiment was conducted to assess the spatial resolution of the radar using closely spaced metallic targets. A flat board with aluminum strips was used to create three configurations with inter-strip spacings of 1cm, 1.25cm, and 2cm. The radar operated at a carrier frequency of 24 GHz, corresponding to a wavelength of approximately 1.25cm ($\lambda = 0.0125$ m).

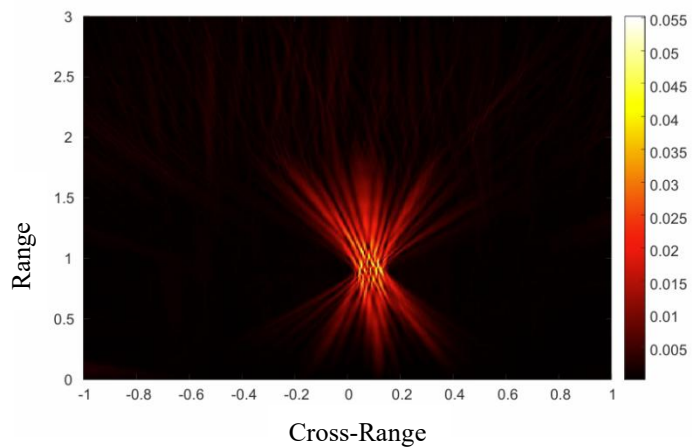
Data was collected for each configuration using the same setup and processing method. The reconstructed images, shown in Figure (4.10) and (4.11) highlight the effect of target spacing relative to the radar wavelength. When the strip spacing (1cm) was smaller than the wavelength, the targets could not be clearly resolved, producing a blurred image. At a spacing (2cm) exceeded the wavelength, the individual targets were distinctly resolved.



(a)



(b)

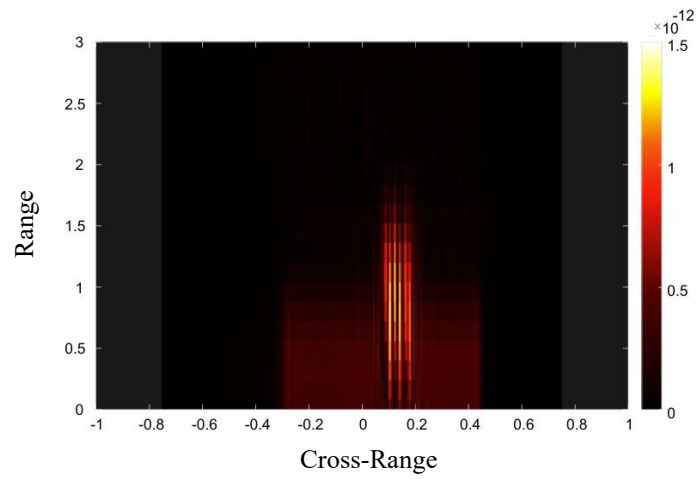


(c)

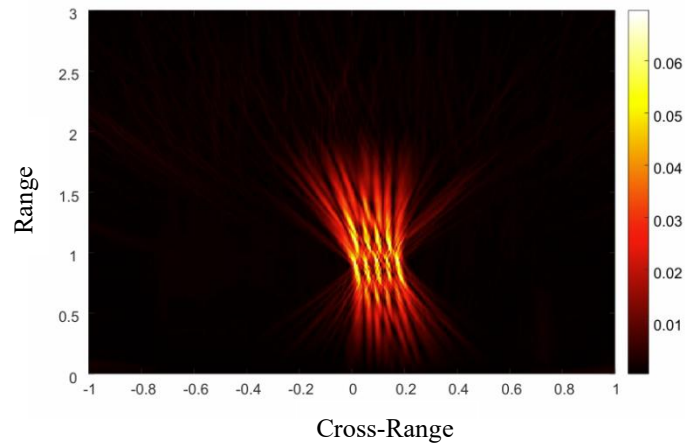
Figure 4.10: Target 1: Reflective surface separated by 1 cm: (a) Reflective surface separated by 1 cm; (b) RDA image; (c) BP image (*figure generated using equations provided by Noah Butler*).



(a)



(b)



(c)

Figure 4.11: Target2: Reflective surface separated by 2 cm; (a) Reflective surface separated by 2 cm; (b) RDA image; (c) BP image (figure generated using equations provided by Noah Butler).

Beamforming for Angular Resolution Enhancement

To enhance the angular resolution of the reconstructed scene, digital beamforming was applied to the collected radar data. In this process, the received signals from each antenna element are coherently combined after being weighted by an angle-dependent complex phase term, referred to as the array factor (AF), given by:

$$AF = \left[-j \frac{2\pi}{\lambda} d_n \sin(\theta(\eta, b)) \right] ,$$

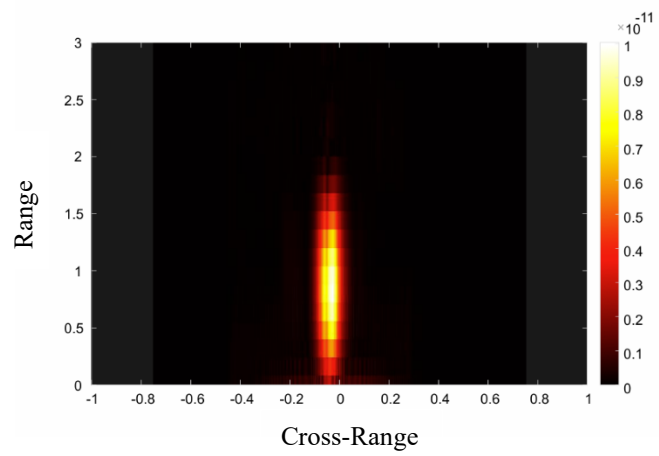
where λ is the radar wavelength, d_{mn} is the spacing between the m^{th} transmitter and the n^{th} receiver, and $\theta(\eta, b)$ denotes the steering angle corresponding to beam index (b) at slow-time sample (η).

The beamformed signal is obtained by summing the weighted signals across all receiver channels:

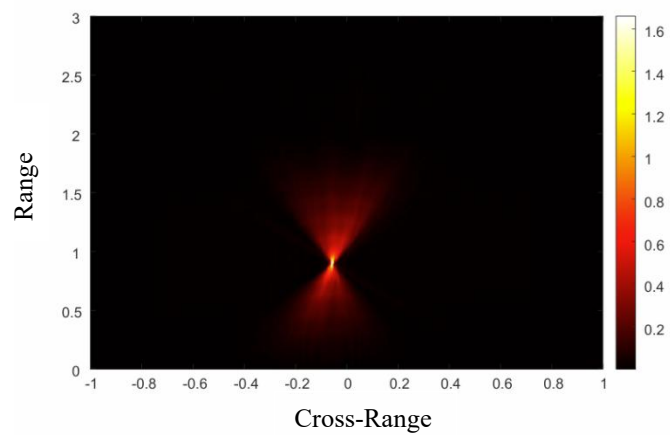
$$S_{BF}(t, \eta, b) = \sum_{n=0}^{N-1} S_{IF}(t, \eta, n) AF(\eta, n, b) , \quad (4.3)$$

where $S_{IF}(t, \eta, n)$ represents the IF signal at the n^{th} receiver, and $S_{BF}(t, \eta, b)$ is the resulting beamspace signal for beam index (b).

Once the data are transformed into the beamspace domain, image formation can proceed by integrating over the focused beams. In this experiment, the signals received from the seven virtual antennas of the TinyRad system were weighted using the array factor to steer the beam toward the center of the scene, thereby improving target localization. Figure (4.12) presents the resulting image, which demonstrates enhanced angular resolution compared to the unfocused case.



(a)



(b)

Figure 4.12: Imaging after Beamforming; (a) Image using RDA; (b) Image using BP (figure generated using equations provided by Noah Butler).

Chapter 5

SUMMARY

This thesis presents the theoretical foundation and experimental validation of a Frequency-Modulated Continuous Wave (FMCW) radar system for target detection and Synthetic Aperture Radar (SAR) imaging. The research focuses on understanding the operational principles of FMCW radar, analyzing its range and velocity measurement capabilities, and extending its functionality to high-resolution imaging through SAR techniques. The thesis provides a comprehensive analysis of FMCW signal generation and processing. It discusses range estimation, and Doppler-based velocity extraction. The thesis also elaborates on the concepts of synthetic aperture formation, and various SAR operation modes such as stripmap, spotlight, and scan.

Two principal imaging algorithms are investigated:

- **Range–Doppler Algorithm (RDA):** A frequency-domain approach that provides computational efficiency through range and azimuth compression with range cell migration correction.
- **Backprojection Algorithm (BPA):** A time-domain technique that delivers better image clarity and flexibility for non-linear platform motion, albeit at higher computational cost.

Experimental Implementation

The experimental work employs two 24 GHz radar modules, a (1Tx-2Rx) and (2Tx-4Rx) systems. A semi-anechoic enclosure was constructed to minimize reflections and simulate a free-space environment. The radar was mounted on a 1.5-meter motorized rail, enabling data acquisition under the stop-and-go assumption at discrete spatial points. The experiments were designed to evaluate range, velocity, and imaging performance.

Range profiles were generated through FFT processing, validating the correct operation of the radar by accurately identifying targets at expected distances. Doppler processing enabled motion estimation and velocity profiling.

Both RDA and BPA were implemented and compared:

- RDA achieved faster computation but exhibited lower spatial resolution.
- BPA produced sharper, well-focused images with improved target definition, confirming its effectiveness for high-fidelity reconstruction.

Experiments on closely spaced metallic targets demonstrated that resolution improves proportionally with wavelength, verifying theoretical predictions. Beamforming techniques were also applied to enhance angular resolution, leveraging virtual array configurations to achieve finer spatial focusing.

5.1 Future Work

The work presented in this study represents the preliminary stage of understanding the fundamental operation of an FMCW radar signal and its application in SAR imaging. The experiments and analyses carried out thus far focused on

developing a baseline digital SAR processing framework, implementing algorithms such as Range–Doppler and Backprojection, and exploring the relationships among system bandwidth, resolution, and imaging performance.

Conventional SAR systems face several challenges, such as limited bandwidth, beam squint, and high Size, Weight, Power, and Cost (SWaP-C). These issues become more pronounced at higher operating frequencies and with larger apertures. Furthermore, the need for high-speed analog-to-digital converters (ADCs), digital-to-analog converters (DACs), and extensive digital signal processing increases system complexity, thereby hindering real-time operation and scalability.

To overcome these limitations, future research aims to translate portions of SAR signal processing into the optical domain. Rather than directly converting received radio frequency (RF) signals into the digital domain, microwave photonics enable their modulation onto optical carriers. This facilitates substantial signal processing and beamforming within the optical domain. Optical systems are inherently lightweight, energy-efficient, and well-suited for broadband and high-frequency applications. Additionally, optical beamforming supports true-time-delay (TTD), which alleviates the bandwidth and beam-squint constraints associated with conventional digital beamforming (DBF). The analog nature of optical processing also minimizes synchronization challenges and latency, resulting in faster and more energy-efficient operation.

Future research will focus on developing photonic-based MIMO SAR systems that utilize Fourier-based opto-electronic architectures. These architectures maintain spatial and temporal coherence independent of the number of antenna elements. In such systems, received RF signals are first converted into optical signals and

subsequently processed using Fourier-transform lenses. These lenses separate and focus the signals according to their angles of arrival, generating an optical pattern at the focal plane that directly represents the target scene [10], [11]. This method substantially reduces digital processing demands and latency while improving energy efficiency, bandwidth capacity, and overall system throughput.

For the initial studies in this area, simulations were carried out on a system where the received beams were weighted using an array factor to steer each receiver’s response toward specific angles. The beam corresponding to the strongest return was then selected for image formation, effectively reducing the computational load during the imaging process. The effect of varying the number of selected beams is visualized below.

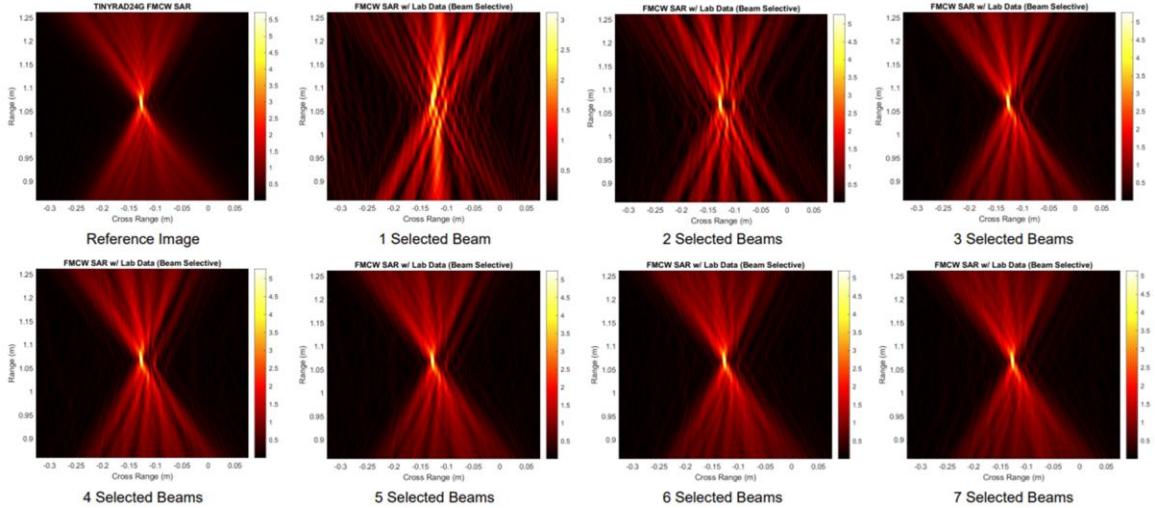


Figure 5.1: Comparison of the reference image with beamspace SAR images formed using 1–7 beams (*Image provided by Noah Butler*).

In addition to improving processing speed and resolution, the next-generation system will employ an optically enabled hybrid stripmap–spotlight SAR configuration. Conventional SAR systems typically operate exclusively in stripmap or spotlight mode. By integrating optical beamforming, it becomes possible to merge the advantages of both. In the proposed configuration, the transmitter will illuminate a broad region, while the optical receiver array forms multiple simultaneous narrow beams across the scene. This stripmap-spotlight hybrid mode enables concurrent wide-area imaging and localized high-resolution observation, allowing adaptive beam selection based on return strength or region of interest [9], [12].

REFERENCES

- [1] Y. Li, “Frequency-modulated continuous-wave synthetic-aperture radar: improvements in signal processing,” Memorial University of Newfoundland, 2016. Accessed: Nov. 12, 2025. [Online]. Available: <https://hdl.handle.net/20.500.14783/9166>
- [2] P. W. Vachon, “Digital Processing of Synthetic Aperture Radar Data: Algorithms and implementation.,” *Geomatica*, vol. 59, no. 3, pp. 353–355, Sept. 2005.
- [3] H. Cruz, M. Véstias, J. Monteiro, H. Neto, and R. P. Duarte, “A Review of Synthetic-Aperture Radar Image Formation Algorithms and Implementations: A Computational Perspective,” *Remote Sensing*, vol. 14, no. 5, p. 1258, Mar. 2022, doi: 10.3390/rs14051258.
- [4] E. C. Zaugg, “Generalized image formation for pulsed and LFM-CW synthetic aperture radar,” Ph.D., Brigham Young University, United States -- Utah, 2010. Accessed: Nov. 12, 2025. [Online]. Available: <https://www.proquest.com/docview/305185095/abstract/A42B3C17E934478DPQ/1>
- [5] A. Parashar, “A Study on Range Cell Migration Correction in SAR Imagery and MATLAB Implementation of Algorithms,” no. 213, 2015.
- [6] A. K. Roy, S. A. Gangal, and C. Bhattacharya, “Demonstration of backprojection algorithm for ISAR image formation with FMCW radar,” in *2016 IEEE International Geoscience and Remote Sensing Symposium (IGARSS)*, July 2016, pp. 1078–1081. doi: 10.1109/IGARSS.2016.7729273.
- [7] M. I. Duersch, “Backprojection for Synthetic Aperture Radar”.
- [8] “MIMO Radar (Rev. A).” Accessed: Nov. 12, 2025. [Online]. Available: <https://www.ti.com/lit/an/swra554a/swra554a.pdf?ts=1762922006399>
- [9] F. Korkmaz and M. Antoniou, “A New Concept of Contiguous-Swath SAR Imaging with High Resolution: Strip-Spot SAR,” *Sensors*, vol. 22, no. 23, p. 9153, Jan. 2022, doi: 10.3390/s22239153.
- [10] S. Shi *et al.*, “Photonic Assisted 2D Transmit Array Using Fourier-Based Beamformer,” in *2024 IEEE International Symposium on Phased Array Systems and Technology (ARRAY)*, Oct. 2024, pp. 1–4. doi: 10.1109/ARRAY58370.2024.10880415.
- [11] D. W. Prather, “The Role of Photonic Devices in Advanced Phased Array Antennas,” in *2025 IEEE International Workshop on Antenna Technology (iWAT)*, Feb. 2025, pp. 1–4. doi: 10.1109/iWAT64079.2025.10931213.

- [12] C. Schuetz, M. Bnyamin, G. Schneider, J. Murakowski, and D. Prather, “Hybrid Strip-Line/Spotlight-Mode SAR Based on Photonic Beamforming,” in *2024 IEEE Conference on Computational Imaging Using Synthetic Apertures (CISA)*, May 2024, pp. 1–4. doi: 10.1109/CISA60639.2024.10576419.